Fifty-Fifty Zr-Ti Solid Solution with a TiO2-Type Structure: Electronic Structure and Photochemical Properties of Zirconium Titanate ZrTiO4

(Article begins on next page)

18 October 2024

iris - AperTO

Fifty-Fifty Zr-Ti Solid Solution with a TiO_2-type Structure: Electronic Structure and Photochemical Properties of Zirconium Titanate $ZrTiO_4$

Valeria Polliotto[¥], Elisa Albanese[¤], Stefano Livraghi[¥], Paulina Indyka[§], Zbigniew Sojka[§], Gianfranco Pacchioni[¤], Elio Giamello[¥]*

[¥] Dipartimento di Chimica and NIS, Università di Torino, Via P. Giuria7, 10125 Torino, ITALY
[¤] Dipartimento di Scienza dei Materiali, Università di Milano Bicocca, Via R. Cozzi 55, 20125 Milano, ITALY
[§] Faculty of Chemistry, Jagiellonian University, 30-060 Krakow, ul. Ingardena 3, POLAND

* elio.giamello@unito.it

ABSTRACT: Polycrystalline zirconium titanate, $ZrTiO_4$, has been prepared via sol-gel chemistry and its properties both as a semiconducting oxide and a photoactive system have been investigated by experimental and computational techniques. The oxide exhibits a structure analogous to those of the main TiO_2 polymorphs with a slightly higher band gap of 3.65 eV. Theoretical results explain this small difference in terms of composition of the lower part of the conduction band which is based on Ti 3d orbitals. Interestingly zirconium titanate is much less reducible than TiO_2 upon annealing under vacuum in the range between room temperature and 673 K. Over this temperature the system releases O_2 forming oxygen vacancies and trapping excess electrons on tetravalent Ti ions as firmly indicated by both Electron Paramagnetic Resonance (EPR) and computational results. Irradiating the solid with UV photons a charge separation is observed by EPR and the photogenerated carriers easily reach the surface where they react with gas phase molecules. $ZrTiO_4$ shows therefore a photochemical behavior very similar to that of TiO_2. Its band potentials, however, slightly differs from those of titania (in particular the conduction band potential is more negative of about 0.20 eV) making the solid of potential interest for further photocatalytic investigations.

1. INTRODUCTION

In order to improve both the processes of pollutants abatement (in particular the area of the so called emerging pollutants) and those related to the production of hydrogen and other solar fuels the development of new photocatalytic materials is mandatory. It should be important, in particular, to develop new generations of photoactive solids capable of going beyond classic titanium dioxide.[1] This latter oxide has in fact excellent properties (stability, non-toxicity, low cost, good oxidation potential of photo-generated holes) but also clear limitations (poor or no activity in the visible light, weak reduction potential of photo-excited electrons). For this reason the search of new oxide systems with superior electronic properties, either bare oxides or oxides doped in various ways, is of vivid scientific interest.[2]

Our groups started few years ago an exploration of new systems relatively unknown to the research in photocatalysis. Our attention points to the investigation of both of the electronic structure of the new materials and their capability of photoinduced charge separation. In the present paper we investigate the properties of zirconium titanate ($ZrTiO_4$), an oxide containing both titanium and zirconium tetravalent ions in equivalent amount.[3] While the properties of TiO_2 have been investigated for more than forty years in photocatalysis,[4] those of ZrO_2 are relatively less studied.[5] However, quite recently this oxide with large band gap value and weak propensity to be reduced, doped with alioelements, has found several applications in photocatalysis.[6-8] It is therefore interesting to explore a system whose stoichiometry is exactly midway between the two oxides.

Zirconium titanate, $ZrTiO_4$, and $ZrTi_2O_6$ or srilankite are the only stable ternary compound in the ZrO_2-TiO_2 phase diagram. They have the same structure (orthorhombic *Pbcn*) which, is very similar to those of all TiO_2 polymorphs being based on TiO_6 octahedra linked by three-coordinated oxygen (the scrutinyite structure, Figure 1). Remarkably the $ZrTiO_4$ phase is stable also over 1200°C.[9-11]

In the structure shown in Figure 1 titanium and zirconium ions are randomly distributed on equivalent octahedral sites and are surrounded by six oxygen atoms. The oxygen atoms are connected to three metals ions.[12]
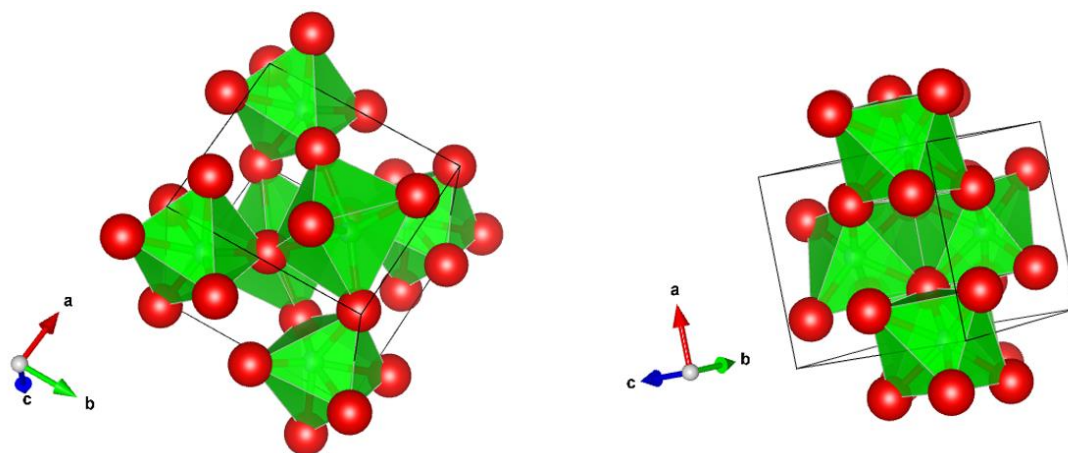
Figure 1. Structure of ZrTiO$_4$. The titanium or zirconium ions are located inside the octahedral constituted by the oxygen ions (red spheres).

ZrTiO$_4$, exhibits many attractive properties including excellent dielectric constant, high corrosion resistance, high permittivity at microwave frequencies and excellent temperature stability.[13-16] For these reasons this material is widely used in technological application, such as in microwave telecommunications (as capacitor, dielectric resonator in filters, and oscillator),[17-18] optical devices,[19] memory devices (ReRAM),[20] humidity sensors,[21] in the manufacture of high temperature pigments,[22] as structural ceramics [16] and, more recently, as biomaterial for medical applications.[23] However, the photochemical/photophysical and redox properties, of ZrTiO$_4$ remain poorly investigated.[24-27]

In our studies concerning new potential photocatalytic materials (mainly metal oxides) we follow a rational approach trying to go beyond the still very popular empiric approaches often found in photocatalytic research. We thus systematically consider a series of key factors potentially influencing the properties of a photoactive solid. The main ones are the electronic structure of the material (band gap energy value, presence of intra band gap states), the band potentials, the behavior under irradiation, and the presence of surface trapping sites for photogenerated charge carriers. The analysis of all these factors is not automatically leading to the identification of materials with superior photocatalytic properties, but is certainly a powerful tool suitable for a preliminary discrimination among a multitude of potentially photocatalytically active systems.

The described approach is based on the coupling of experimental techniques and advanced theoretical calculations. Optical spectroscopy and Electron Paramagnetic Resonance, in particular,

monitor the energy gap of the solid, the formation of reduced states upon particular treatments (reducible oxides) and that of charge carriers upon irradiation. Computational results allow an accurate description of the geometrical and electronic properties of the investigated material and a reliable study of the defects formed when the system is partially reduced. As it will be shown in the following, $ZrTiO_4$ is an example of a solid oxide that, either bare or suitably doped with hetero-elements, has promising potential applications as photocatalytic material.

2. EXPERIMENTAL SECTION

Sample preparation: The $ZrTiO_4$ (hereafter ZT) powder was prepared via sol-gel technique, mixing a solution of 3.5 mL of titanium(IV) isopropoxide and 5 mL of zirconium(IV) propoxide (molar ratio 1:1) in 9mL of 2-propanol alcohol to which 3.5 mL of water were added. The gel was left to age for 15 hours at 290 K and subsequently dried at 343 K. The dried material was calcined in air at 973 K for 1 hour. The powder presented a white color.

X-Ray Diffraction: Powder X-ray diffraction (XRD) pattern was recorded with a PANalytical PW3040/60 X'Pert PRO MPD diffractometer using a copper Ka radiation source (0.154056 nm). The intensities were obtained in the 2θ range between 20° and 80°. X'Pert High-Score software was used for data handling.

UV-vis absorbance: The UV-vis absorption spectra were recorded using a Varian Cary 5 spectrometer, coupled with an integration sphere for diffuse reflectance studies, using a Carywin-UV/scan software. A sample of PTFE with 100% reflectance was used as the reference.

Surface area measurements: The surface area measurement was carried out on a Micromeritics ASAP 2020 apparatus using the Brunauer–Emmett–Teller (BET) model for N_2 adsorption measurements. Prior to the adsorption run, the sample was outgassed at 573 K for 2 h.

UV-vis irradiation: The samples were irradiated with UV-vis light using a 1600 W xenon lamp (Oriel instruments) equipped with a IR water filter. The effect of irradiation on EPR spectra was investigated irradiating the sample in the EPR cavity at 77 K.

EPR characterization: Continuous Wave Electron paramagnetic resonance (CW-EPR) experiments were performed with a Bruker EMX spectrometer operating at X-band (9.5 GHz), equipped with a cylindrical cavity operating at 100 kHz field modulation. All the spectra were recorded with a Modulation Amplitude 0.2 mT and at 77 K. Other experimental parameters are

reported in the captions of the figures. Before every experiment the sample was subjected to an activation process: the samples was heated for 30 minutes at 773 K (283 K/min) under vacuum and other 60 minutes in 20 mbar of O_2.

Trasmission Electron Microscopy analysis: The nanoscale TEM imaging of the samples was performed using a high-resolution transmission microscope Tecnai Orisis (FEI) with a X-FEG Schottky field emitter, operated at the accelerating voltage of 200 keV. For chemical composition analyses a windowless Energy Dispersive X-ray (EDX) system with a 4-sector silicon drift detector (SDD) was used. The Z-contrast images were acquired by means of a high angle annular dark field (HAADF) detector in the scanning mode (STEM). The STEM images coupled with the EDX elemental mapping were acquired including the sample drift correction using the Bruker Esprit software. Prior to microscopic analysis, the samples were ultrasonically dispersed in ethanol and dropped on a holey carbon film supported on a copper grid (Agar Scientific, 300 mesh). Analysis of the observed TEM images was corroborated by the computer image simulations by means of the multi-slice method implemented in the JEMS software.[28] The Poisson noise at the level of 10% of the total contrast was added to the simulated images, in order to approach the experimental imaging conditions. To confirm the crystal phase assignment and reveal the orientation of crystallites, a single crystal diffraction pattern was simulated (within the kinematical and dynamical approximation) by means of the Rhodius software.[29-30]

DFT calculation: The investigation of $ZrTiO_4$ was carried out with periodic DFT calculations employing the Becke-3 [31] and Lee-Yang-Parr [32] (B3LYP) exchange and correlation functional as implemented in the CRYSTAL14 program.[33]

Crystalline orbitals were represented as linear combinations of Bloch functions (BF) and were evaluated over a regular three-dimensions mesh of points in reciprocal space. Each BF was built from local atomic orbitals (AO) resulting from contractions (i.e. linear combinations with constant coefficients) of Gaussian-type functions, which in turn are the product of a Gaussian times a real solid spherical harmonic function. All electron basis sets for O (8-411(d1)) and Ti (86-411(d41)) have been used. For Zr atoms, a 311(d1) basis set associated to ECP (Hay and Wadt small-core potential) has been selected. For the numerical integration of exchange-correlation term, 75 radial points and 974 angular points (XLGRID) in a Lebedev scheme in the region of chemical interest were adopted. The Pack-Monkhorst/Gilat shrinking factors for the reciprocal space were set to 3

for all the structures, which correspond to 14 real reciprocal space points at which the Hamiltonian matrix was diagonalized.

The calculations of the $ZrTiO_4$ structures were performed on a 96 atoms supercell, corresponding to a 2x2x2 unit cell of orthorhombic $ZrTiO_4$. The accuracy of the integral calculations was increased with respect to its default value by setting the tolerances to 7, 7, 7, 7 and 18. The self-consistent field (SCF) iterative procedure converged to a tolerance in total energy of $\Delta E = 1 \cdot 10^{-6}$ a.u. The above computational parameters ensured a full numerical convergence on all the computed properties described in this work. All the crystal structures are fully optimized (i.e. both cell parameters and internal coordinates) without symmetry operators in order to allow a complete structural relaxation.

3. RESULTS AND DISCUSSION

3.1. *Structural and optical characterizations.*

XRD analysis was performed for the ZT powder and the corresponding XRD patterns is reported in Figure 2 (black line) together with the diffraction lines of a reference $ZrTiO_4$ (red lines). All the peaks of the diffraction pattern of our sample correspond the $ZrTiO_4$ phase.

The surface area of the ZT sample measured using the BET method corresponds to 66 m^2/g.

The optical absorption in the UV and visible region of ZT is shown in Figure 3. The inset of Figure 3 shows the Tauc's plot of the optical absorption spectrum measured at room temperature in order to evaluate the experimental band gap value. According to the Tauc's relation, the absorption coefficient α for direct band gap materials is given by

$$\alpha(h\nu) = B(h\nu - E_g)^m \quad (1)$$

where B is an energy independent constant, α is the absorption coefficient, E_g is the optical band gap energy, h is the Planck's constant, ν is the frequency of the incident photon and m is an index that depends on the nature of electronic transition responsible for the optical absorption. Values of m for the allowed direct and non-direct transitions are 1/2 and 2, respectively. In the present case the electronic bands are almost flat (see Figure S1 in Supporting Information), pointing to a direct band gap oxide. The optical band gap energy evaluated using the Tauc's plot for a direct transition is 3.65 eV, which corresponds to about 340 nm. The optically detected band gap value is

intermediate between that of the two binary oxides of reference (TiO$_2$, ZrO$_2$) but actually closer to that of anatase (3.2 eV).
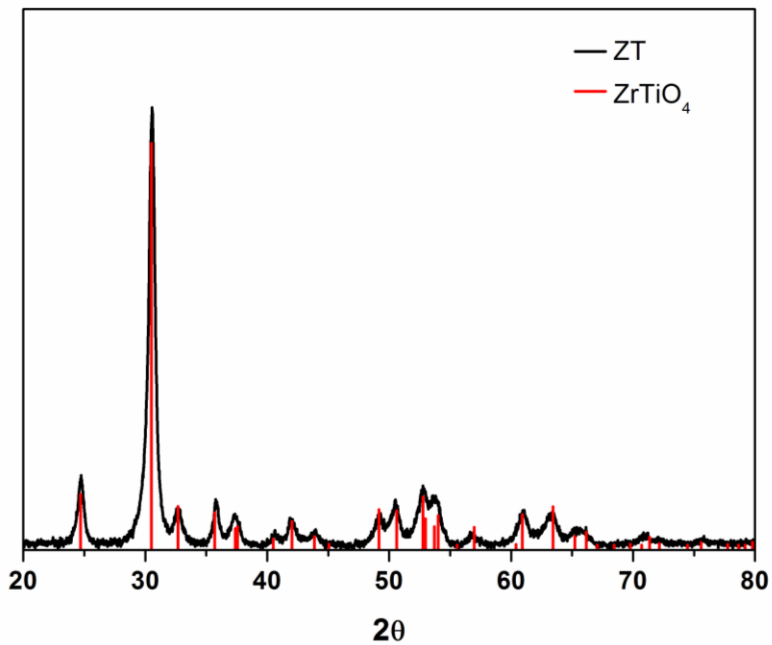

Figure 2. X-Ray diffraction patterns of ZT (black line) and reference of ZrTiO$_4$ (red lines).[34]
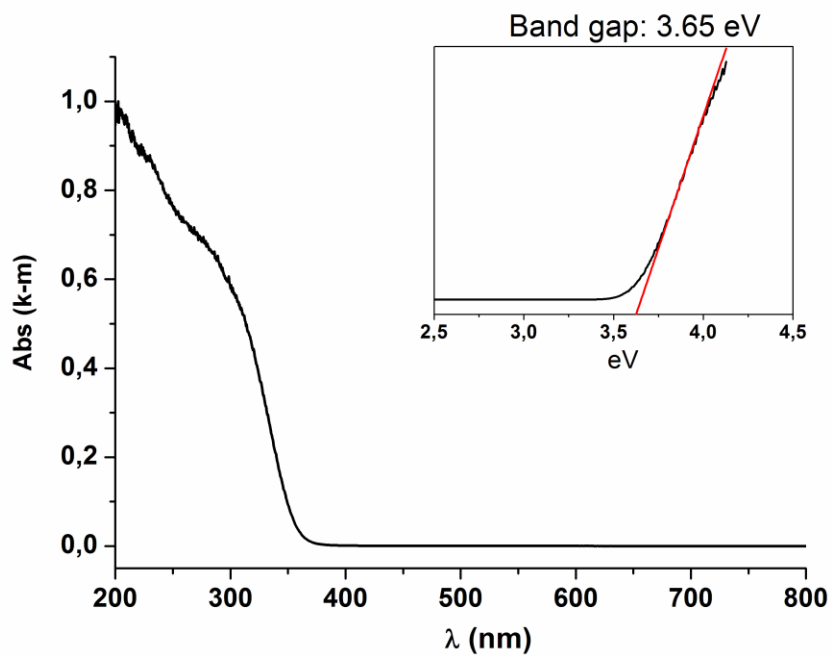

Figure 3. UV-vis diffuse reflectance spectrum of ZT powder. In the inset the Tauc's plot is reported.

3.2. Transmission Electron Microscopy analysis.

The survey and high magnification TEM images shown in Figure 4a and 4b reveal the morphology and structure of the synthesized $ZrTiO_4$ nanoparticles. They exhibit rounded shape with a rather narrow grain size distribution with the average diameter of about 15 nm in accordance with the Scherrer analysis of the XRD pattern. The nanoparticles are aggregated into elongated structures that form globular submicron agglomerates (Figure 4a). The corresponding selected area electron diffraction (SAED) pattern shows their polycrystalline nature (Figure 4c). The observed diffraction rings were indexed within the orthorhombic structure of $ZrTiO_4$ (space group *Pbcn*), and they correspond well with the reference JCPDS diffraction pattern No. 34-415.
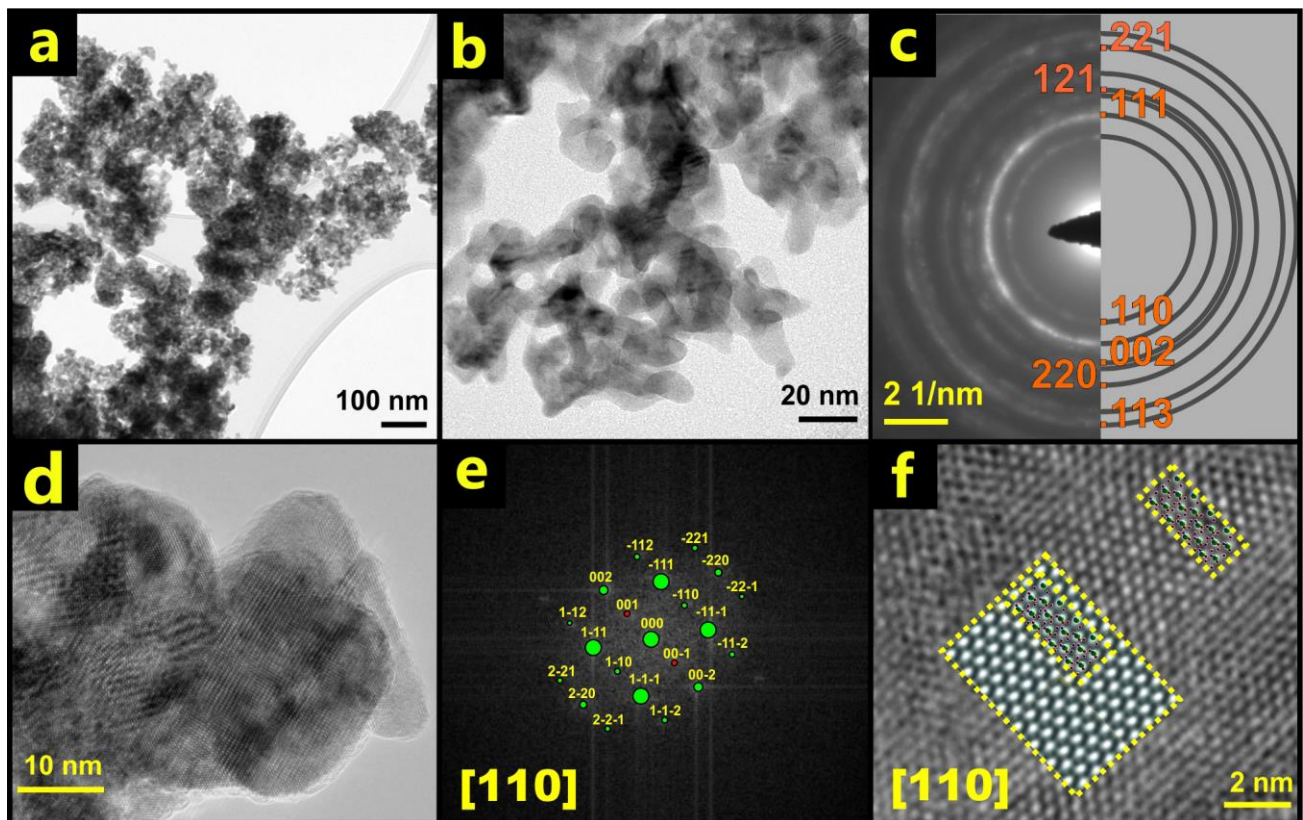

Figure 4. TEM images of the $ZrTiO_4$ nanostructures (a, b) along with the polycrystalline electron diffraction SAED pattern (c). High resolution image of the nanocrystallites (d), and FFT pattern taken from the HR TEM image viewed along the [110] direction with the superimposed simulated single crystal diffraction pattern (e). The simulation was carried out taking into account kinematical (green dots) and dynamical (red dots) scattering. HR TEM image of the orthorhombic $ZrTiO_4$ nanoparticle oriented along the [110] axis (f) together with the simulated image (yellow rectangle) and the superimposed atomistic structure of $ZrTiO_4$ (Zr – green dots, Ti – blue dots, O – red dots).

A high degree of crystallinity of the $ZrTiO_4$ nanograins was confirmed by the HR-TEM imaging, which shows the presence of ordered lattice fringes (Figure 4d). Simulation of the FFT diffraction pattern, taking into account both the kinematical (green circles) and the dynamical effects, (red circles corresponding to the (001) and (00-1) reflections), enabled straightforward assignment of the all observed diffraction spots, and determination of the nanocrystal alignment along the [110] direction. The corresponding HR TEM image was next simulated (Figure 4f) within the extended Scherzer defocus regime and the spherical aberration constant C_s = 12 µm. The simulated image matches perfectly the experimental one, allowing for univocal contrast interpretation. Analysis of the calculated thickness - defocus maps showed that the observed nanocrystal has the thickness of ~ 8 nm. Within the applied imaging conditions, the bright spots define the positions of the mixed zirconium and titanium columns, whereas oxygen columns remain invisible.
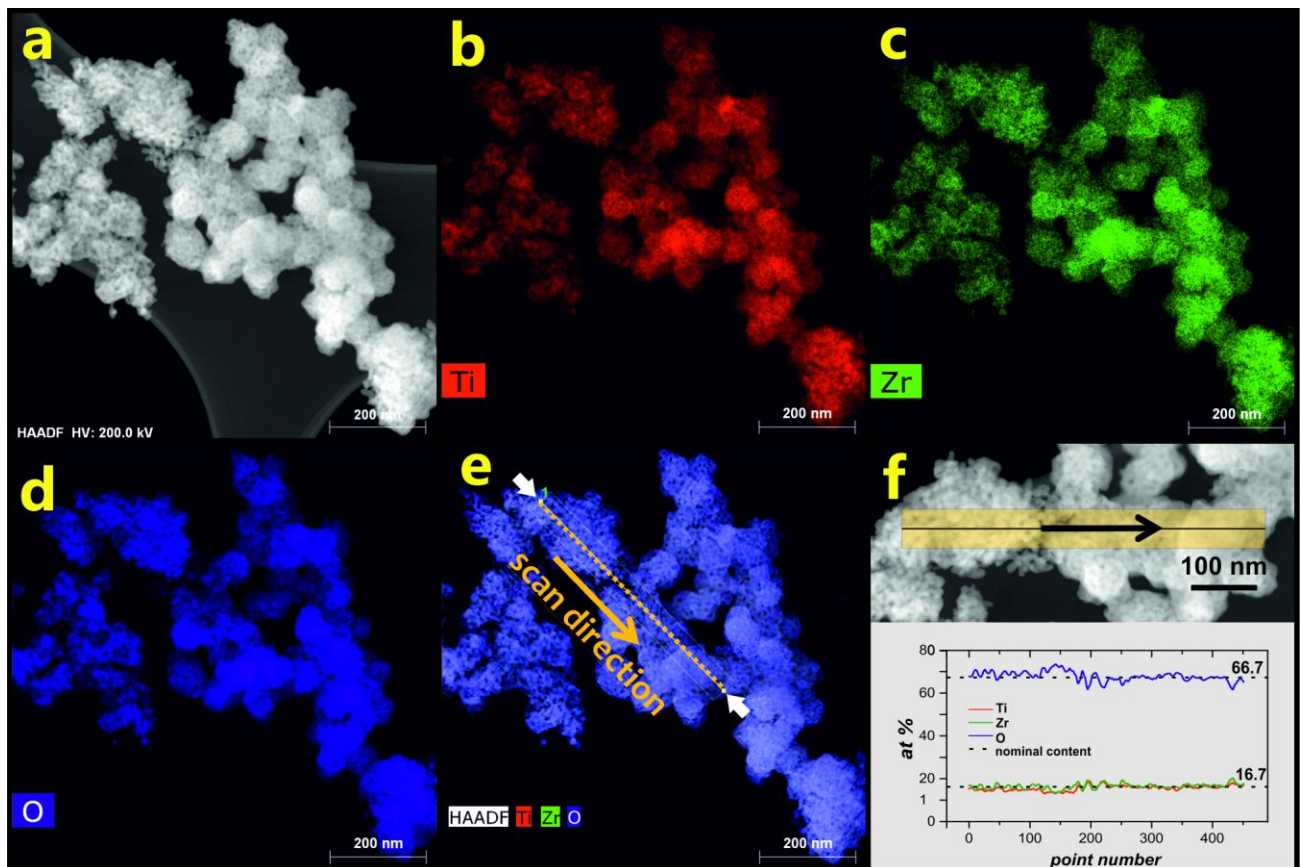

Figure 5. STEM-HAADF image of the $ZrTiO_4$ nanostructures (a) along with EDX maps (b-d) showing distribution of the constituting elements Ti (red), Zr (green), and O (blue). EDX line profile across the $ZrTiO_4$ aggregates (e) and the corresponding variation of the composition (f).

In order to examine the composition homogeneity of the samples at submicro and nanoscales HAADF/STEM pictures (Figure 5a) and the associated EDX maps were reported (Figure 5b,c,d). Inspection of the results shows a very homogeneous distribution of the constituent Zr, Ti and O elements, and absence of any locally segregated TiO_2 or ZrO_2 phase impurities. A more accurate EDX profile analysis along the linescan direction marked in Figure 5e clearly confirmed the 1:1:4 stoichiometry of $ZrTiO_4$ (the data were quantified using 2 by 2 pixel binning and 5 pixel averaging). However, small fluctuations of the Ti and O content were observed, especially upon passing from the globular aggregates into loosely bound nanoparticles (Figure 5f). The unraveled minute titanium deficiency and the corresponding oxygen excess reached the maximum value of –2.5 at%, +3.6 at% for Ti and O, respectively (left part of the plot). For the compacted aggregates the stoichiometry of $ZrTiO_4$ is well preserved for the majority of the nanostructures (right part of the plot).

Summarizing, the obtained microscopic results revealed good homogeneity and crystallinity of the synthesized material. The $ZrTiO_4$ nanocrystals are of 10-20 nm in size and form globular aggregates of 100-200 nm in diameter.

3.3.   *DFT calculations.*

3.3.1.   *Geometrical and Electronic Structure.*

In the experimental unit cell there is only one non-equivalent cation (M = Zr or Ti) and one non-equivallent anion site (tricoordinated O_{3c}). In the case of $ZrTiO_4$, Ti and Zr atoms occupy randomly half of the cation octahedral positions. This has been modeled with a 96-atoms supercell. Four different $ZrTiO_4$ configurations have been taken into account; one is characterized by segregated Zr and Ti atoms (1-$ZrTiO_4$, Ti and Zr ions occupy distinct parts of the cell without any mixing), while the others three contain dispersed Ti and Zr ions in the octahedral sites (2-, 3-, 4-$ZrTiO_4$) (for the cations distribution in 1-, 2-, 3-, and 4-$ZrTiO_4$ see Figure S2 in Supporting Information). The 1-$ZrTiO_4$ shows a significant expansion of the unit cell (Table 1) due to the segregation of the Zr atoms (see below); on the contrary, the dispersed configurations exhibit smaller changes of the unit cell axes. In particular, the mean cell parameters of 2-$ZrTiO_4$ are in very good agreement with the experimental ones (the difference is always < 1.1%). The dispersed configurations are more stable than the segregated one of about 0.22 eV per unit formula (uf) (i.e.

10

3.4 eV per supercell, see Table 1), consistent with the experimental observations. The relative stabilities of the dispersed structures are very similar (< 0.1 eV/uf), with the 2-ZrTiO$_4$ being slightly more stable than all the dispersed configurations (Table 1). Therefore, in the following we discuss this configuration (Figure 6).
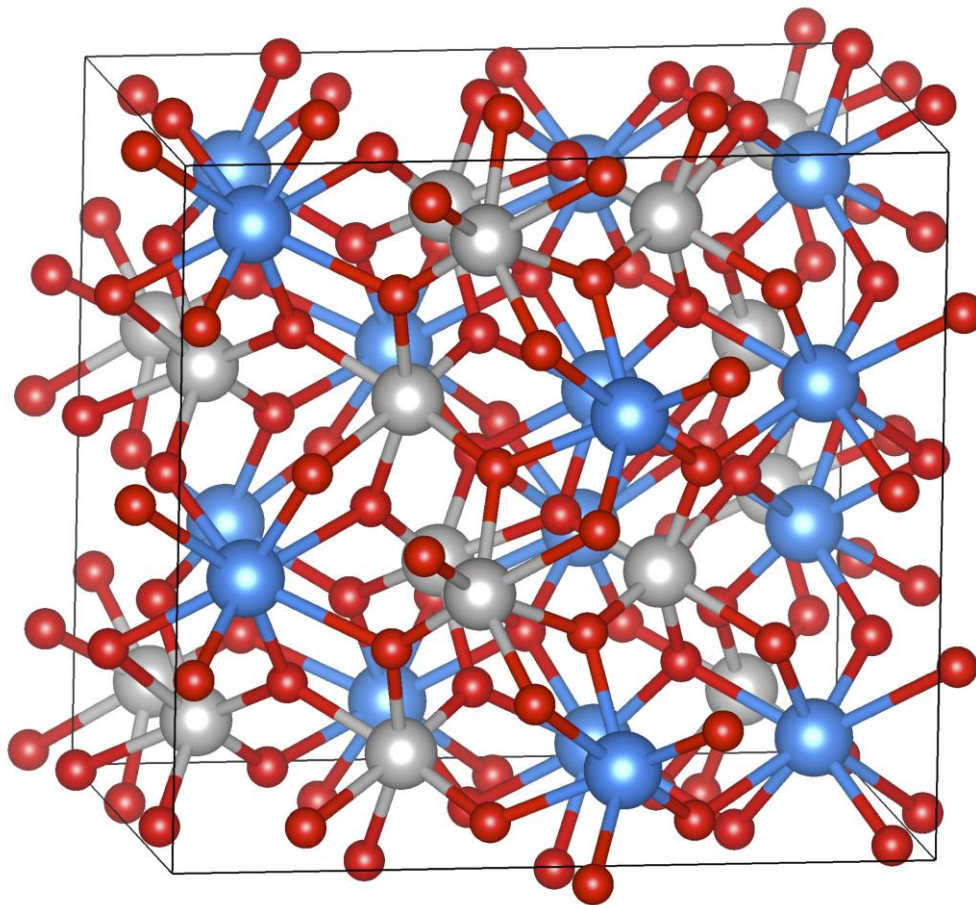

Figure 6. 2x2x2Supercell of 2-ZrTiO$_4$. Ti atoms are in gray, Zr in light blue and O in red.

After the optimization, a strong structural rearrangement is observed. Different O sites have been generated depending on their first neighbors (Figure 7). In particular, the O$_{3c}$ directly bound to three Zr ions change their coordination sphere by attracting a nearby Ti ion and thus forming a distorted tetrahedron O$_{4c}$ (3Zr1Ti). Moreover, the M—O distances show a relevant variation with respect to the experimental data (Figure 7); TiO$_6$ centers report an average Ti—O shortening by 0.7 %, whereas Zr—O bonds are elongated by about 7.0 % (Figure 7).
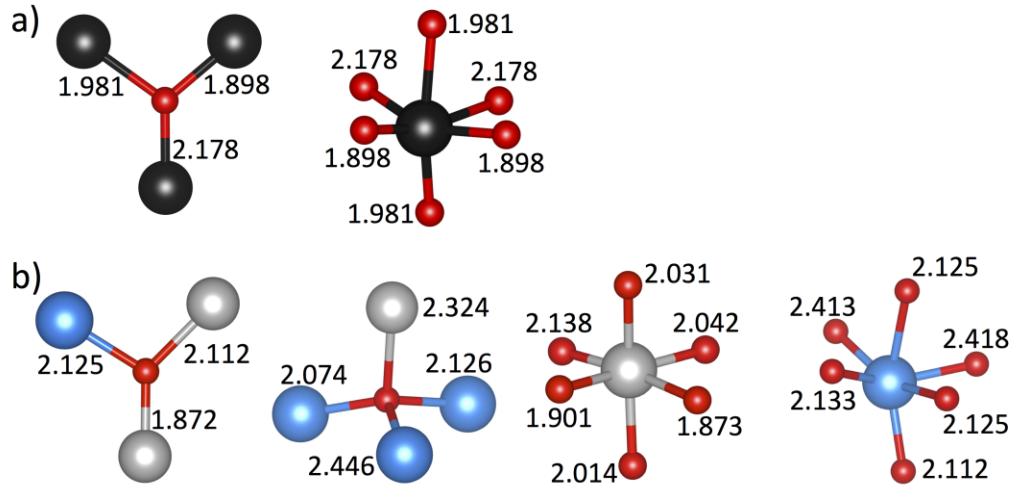
Figure 7. Local structural features of (a) experimental geometry, where the black spheres represent M atoms (M= Zr or Ti) and of (b) the simulated 2-ZrTiO$_4$ structure, where gray represents Ti atoms, light blue Zr and red O.

Table 1: Mean cell parameters (Å), differences (Δ%) with respect to the experimental values [35] and minimum band gap (value obtained at Γ point is in the brackets) of TiO$_2$ anatase, monoclinic ZrO$_2$ and of experimental ZrTiO$_4$ and of Zr$_{(2-x)}$Ti$_x$O$_4$ structures at different compositions (x = 2, 0, 1). The relative stabilities of the four ZrTiO$_4$ configurations (eV per unit formula) with respect to the most stable one (2-ZrTiO$_4$) are also reported.

	a		b		c		E$_g$(eV)	ΔE(eV/uf)
ZrO$_2$	5.240		5.265		5.417		5.73	
TiO$_2$	3.789		3.789		9.776		3.87	
		Δ%		Δ%		Δ%		
Expt ZrTiO$_4$	4.807		5.479		5.034		3.65	
Ti$_2$O$_4$	4.578	-4.8	5.574	+1.7	4.926	-2.1	4.27	
Zr$_2$O$_4$	5.053	+5.1	5.794	+5.7	5.283	+4.9	5.94 (6.13)	
1-ZrTiO$_4$	4.776	-0.6	5.739	+4.7	5.133	+2.0	4.18 (4.20)	+0.21
2-ZrTiO$_4$	4.860	+1.1	5.515	+0.7	5.078	+0.9	4.76 (4.78)	0.0
3-ZrTiO$_4$	4.840	+0.9	5.684	+3.7	5.090	+1.1	4.71 (4.74)	+0.09
4-ZrTiO$_4$	4.881	+1.5	5.598	+2.2	5.061	+0.5	4.73 (4.78)	+0.05

Figure 8 shows the projected density of states (PDOS) of 2-ZrTiO$_4$. As expected, the top of the valence band (VB) is characterized by O 2p states, whereas the bottom of the conducting band (CB)

is characterized by the empty Ti 3d states. It is worth to note that the Ti 3d states lie at lower energy (in the range 4.7-6.0 eV above the top of the VB) than the Zr 4d states (6.2-8 eV). By comparing the DOS curves of 2-ZrTiO$_4$ with those of pure TiO$_2$ and ZrO$_2$ one can conclude that the relative positions of Ti and Zr empty d states are almost unchanged.
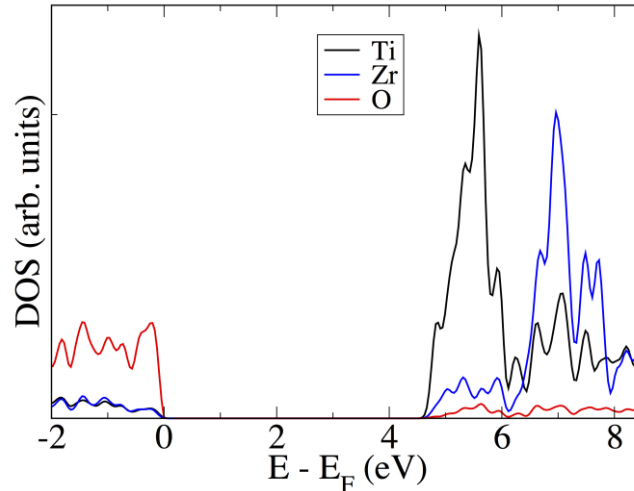

Figure 8. PDOS of 2-ZrTiO$_4$. O contribution to the DOS is represented in red, Ti contribution in black and Zr contribution in blue. The Fermi level is set to the top of the valence band.

The experimental band gap (E_g = 3.65 eV) is 13% larger than that of TiO$_2$ (3.2 eV, see Table 1). E_g computed for 2-ZrTiO$_4$ with the present method, 4.76 eV, is 23% larger than that of anatase TiO$_2$ computed at the same computational level E_g = 3.87 eV, Table 1. To better understand the origin of the overestimate, the end-members of the Zr$_{(2-x)}$Ti$_x$O$_4$ solid solution were simulated, i.e. x_{Ti}=2 and x_{Ti}=0. A ZrTiO$_4$ structure with only Zr atoms, Zr$_2$O$_4$, has E_g = 5.94 eV, which is close to the computed ZrO$_2$ value (for the monoclinic polymorph E_g = 5.73 eV) and in good agreement with the experimental values (range 5.8-6.2 eV).[36] On the contrary, Ti$_2$O$_4$ (E_g = 4.27 eV) has a band gap significantly higher (10%) than the anatase TiO$_2$ (3.87 eV, to be compared with the experimental value of 3.2 eV [37]). The overestimation of the calculated ZrTiO$_4$ band gap is then related to the Ti component, whose computed 3d empty states lie at relatively high energies due to structural effects. Thus, the calculations correctly reproduce the shift of the band gap observed experimentally. The absolute values are too large due to the fact that the B3LYP functional tends, in the case of TiO$_2$, to overestimate the band gap (by about 21%, Table 1). If we apply this correction and reduce the computed band gap of 2-ZrTiO$_4$ by 21%, we obtain the value of 3.8 eV, close to the measured E_g. In conclusion, in ZrTiO$_4$, the nature of VB and of the bottom of CB is very

similar to that of TiO_2 and the small increase of the band gap is due to geometrical effects that lead to a widening of the gap.

3.3.2. Oxygen Vacancy.

The nature of the oxygen vacancies (V_O) and the fate of the two electrons left in the solid when the vacancy is created have been investigated by simulating several $ZrTiO_{4-x}$ defective structures. The presence of different oxygen species in $2\text{-}ZrTiO_4$ requires to remove O atoms from various lattice sites in order to have a complete overview of the stability and electronic behavior of V_O. In particular, two different V_{O3c} and one V_{O4c} have been modeled. The two V_{O3c} centers are surrounded by two Ti and one Zr ions (V_{O3c}-2Ti1Zr) and by two Zr and one Ti ions (V_{O3c}-1Ti2Zr), respectively; whereas the first coordination sphere of V_{O4c} is characterized by two Ti and two Zr ions (V_{O4c}-2Ti2Zr). We discuss the three cases in the following.

V_{O3c}-2Ti1Zr. In principle, several electronic configurations are possible; the two excess electrons can occupy the 3d states of Ti atoms, the 4d levels of Zr atoms or can be trapped in the vacancy (F center). We have tried various possible triplet (T) solutions but only one is found to be stable; it is characterized by two unpaired electrons fully localized on the two undercoordinated Ti cations near the vacancy. The singlet solution (S), where the electrons are trapped in the vacancy, is higher in energy by more than 1.4 eV (see Table 2). This behavior perfectly matches with that of the oxygen vacancy in TiO_2 reported in previous works.[38]

V_{O3c}-1Ti2Zr. In this structure only one Ti is directly connected to the vacancy. The triplet state corresponds to one electron localized on Ti and the other on Zr (see Figure 9). This distribution with one electron in the high-lying Zr 4d orbital has the effect to destabilize the structure, which indeed is 0.8 eV higher in energy than the other tri-coordinated vacancy, V_{O3c}-2Ti1Zr. The other effect is that the triplet state is almost degenerate with the singlet solution, which is actually 0.05 eV more stable. This is consistent with the different nature of the oxygen vacancy in ZrO_2 (two electrons localized in the vacancy) with respect to TiO_2 (two Ti ions reduced to Ti^{3+}).[39]

V_{O4c}-2Ti2Zr. By analyzing the structure and electronic properties of the four-coordinated vacancy, it is clear that the nature of V_O is very similar to that of V_{O3c}-2Ti1Zr (T). The two electrons are, indeed, fully localized on the two under-coordinated Ti ions and the stability is very close to that of V_{O3c}-2Ti1Zr (T) (Table 2).

In summary, we have found three situations, the lowest in energy corresponding to two excess electrons localized on Ti ions (triplet state), and two configurations higher in energy, one with one electron on Ti and one on Zr (triplet state), and the other one with two electrons trapped in the cavity (singlet state). We can conclude that the defective $ZrTiO_{4-x}$ behaves like TiO_{2-x}, with reduction of the Ti ions and formation of Ti^{3+} species.
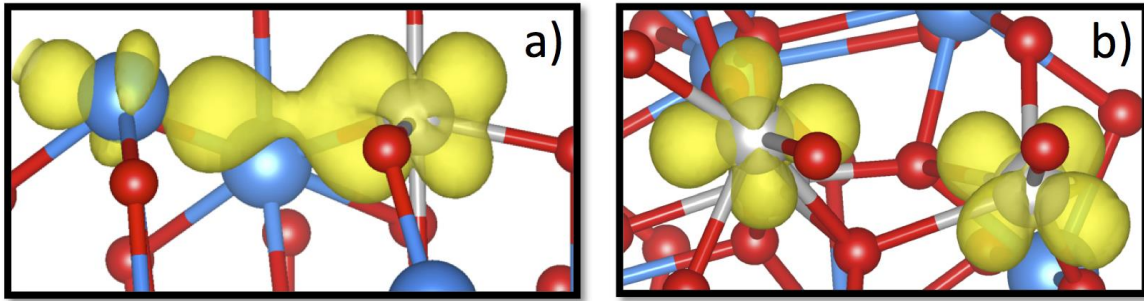

Figure 9. (a) Spin density of V_{O3c}-1Ti2Zr (T) and (b) of the most stable defective structure V_{O3c}-2Ti1Zr (T) (isolevel cutoff set to 0.008).

Table 2. Spin densities (ρ) and relative stabilities (ΔE in eV) of the different electronic configurations of the V_O structures with respect to the most stable one (V_{O3c}-2Ti1Zr (T)).

		ρ				ΔE
		Ti	Ti	Zr	Zr	
V_{O3c}-2Ti1Zr	T	0.95	0.93	0.0		0.0
	S					1.42
V_{O3c}-1Ti2Zr	T		1.11	0.58	0.0	0.78
	S					0.73
V_{O4c}-2Ti2Zr	T	0.93	0.89	0.0	0.0	0.15

*3.4.   Redox and photophysical properties.*

3.4.1.   Reducibility upon annealing: EPR investigation.

Annealing treatments of $ZrTiO_4$ were performed under vacuum at different temperatures for 1h from 373 K to 873 K. In the case of reducible oxides this type of treatment induces a loss of oxygen and generates, beside oxygen vacancies, two extra electrons per vacancy.[40] In the case of a MO_2 oxide, for example, one has

$$MO_2 \rightarrow MO_{2-x} + \frac{x}{2}O_2 + xV_O^{\cdot\cdot} + 2e^- \qquad (2)$$
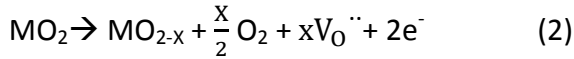
The EPR spectra after annealing of the ZT sample are reported in Figure 10.

To understand the experiment here reported it is useful to recall that pure TiO_2 and ZrO_2 have a rather different behavior in similar experiments. TiO_2 is very sensitive to annealing as it forms reduced Ti^{3+} species at the early stages of the annealing process according to the equation 3.[41]

$$2Ti^{4+} + 2e^- \rightarrow 2\ Ti^{3+} \qquad (3)$$
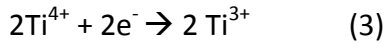
ZrO_2 is more reluctant to reduction with respect to TiO_2. Furthermore, the majority of extra electrons, formed upon annealing, are not EPR visible (in other words only a minor fraction of these electrons forms Zr^{3+} ions).[39] This is consistent with theoretical calculations that show that the oxygen vacancy in bulk ZrO_2 leads to a pair of electrons trapped in the vacancy in a singlet, hence EPR silent, ground state. Localization of the excess electrons associated to an oxygen vacancy on Zr ions (Zr^{3+}) probably occurs only in connection to low-coordinated Zr ions whose electronic states are lower in energy.

The behavior of ZT in the early stages of annealing is more similar to that of ZrO_2 than to that of titania. The EPR spectrum of ZT (Figure 10) (that contains tiny amount Zr^{3+} defects in the starting material having $g_{//}$ =1.978 and $g_\perp$ =1.960, analogously to what occurs in pure ZrO_2 [39]) remains almost unchanged upon annealing stepwise till 573 K except for the tiny spectral component at g=2.003 which increases with the annealing temperature. As in the case of the parent oxides (TiO_2 and ZrO_2) such feature is related to trapped electrons and similarly to what happened in TiO_2 and ZrO_2 they represent only a very minor fraction of the overall reduced states observed via EPR. [39, 41]

Contacting the surface of the anneled ZT sample with O_2 after each step no electron transfer to oxygen is observed suggesting that annealing under vacuum until this temperature does not modify the solid which, in spite of its band gap close to that of TiO_2, is much more resistant to reduction than titania. This is consistent with the computed vacancy formation energies. ΔE of $ZrTiO_4$, equal to about 6 eV, is in fact relatively high and close to that of ZrO_2 (7.2 eV) [39, 42] while

forming a vacancy in bulk TiO_2 has a smaller energy cost (4.5 eV). Upon annealing at 673 K the EPR signal is still almost unaltered however an initial reduction in the solid has occurred as indicated in Figure 11, showing that when the material is contacted with oxygen it gives rise, by electron transfer, to the well-known signal of the O_2^- superoxide anion (Figure 11b). The material, annealed at 673 K, is thus initially reduced in these conditions but there is no EPR evidence of the localized excess electrons (Ti^{3+}, Zr^{3+}), which must therefore be present as diamagnetic centers, most probably, as suggested by calculations as V_O^x neutral centers with two electrons in a vacancy (Section 3.3.2). In anycase, till an annealing temperature of 673 K, the behavior of the ZT system is closer to that of ZrO_2.

The behavior changes upon annealing at higher temperature when the reluctance to oxygen release breaks down.
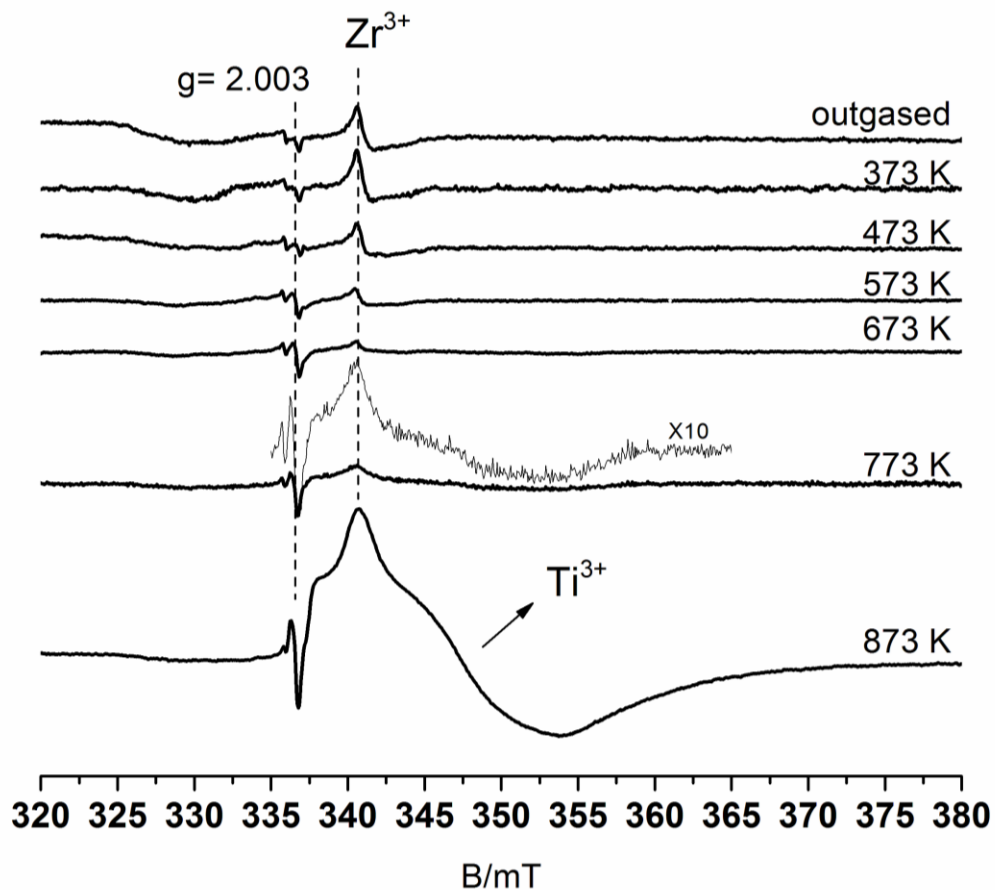

Figure 10. EPR spectra of ZT powder outgased at room temperature and after annealing for 1 hour under vacuum at the temperature indicated in the figure. All the spectra were recorded at 77 K at 10 mW.

17

Already at 773 K, but more evidently at 883 K, a broad signal (around $g=1.93$) is observed for the annealed solid. The latter is remarkably similar to that observed in the case of TiO_2 even at lower annealing temperature and definitely assigned to Ti^{3+} ions in the disordered environment of the nanocrystal surface.[41] This evidence unambiguously indicates the presence of extra electrons in the solid produced upon O_2 release (equations 2 and 3).

No similar signal was ever observed for ZrO_2. According to the computed density of states reported above, the empty Ti 3d levels are lower in energy than the Zr 4d ones and therefore excess electronic charge accumulates on titanium ions.

Zirconium titanate therefore behaves more similarly to ZrO_2 in weak and mild annealing conditions, whereas its resistance to reduction decreases at T > 773 K when it behaves like TiO_2 forming important amounts of surface Ti^{3+} ions.
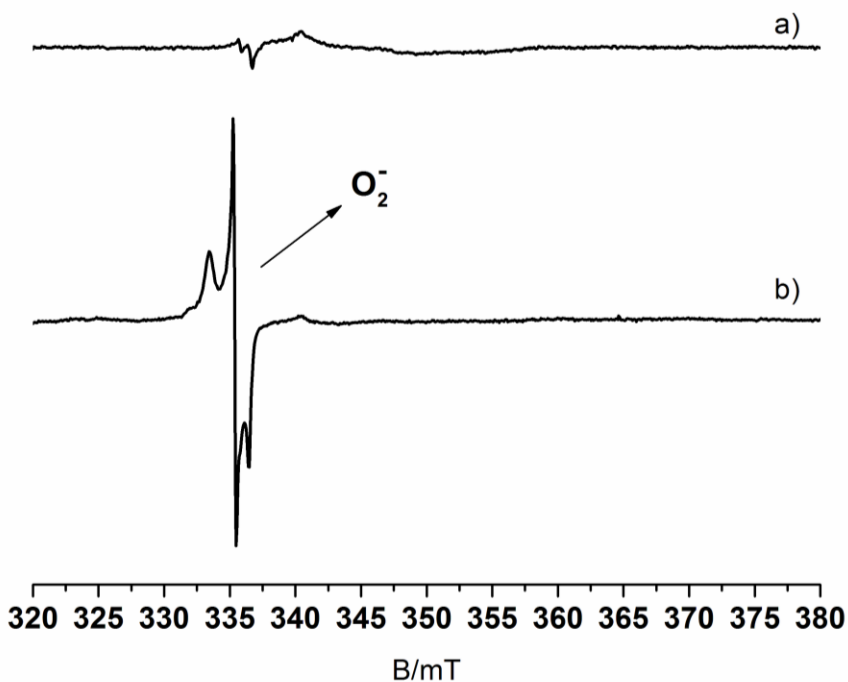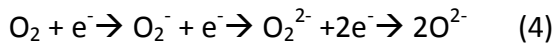

Figure 11. EPR spectra of a) ZT powder reduced 1 hour at 673 K under vacuum and b) after contact with 20 mbar of O_2 at RT. Both spectra were recorded at 77 K and with a microwave power of 10 mW.

Contacting the fully annealed solid with oxygen at room temperature (Figure 12a) the broad, intense signal belonging to the Ti^{3+} centers, instantaneously, disappears and the signal of the

superoxide O_2^- ions is again generated by an electron transfer. The features of the EPR spectrum of the superoxide radical (Figure 13) are characterized by a g_z region with two resolved components indicating the presence of O_2^- adsorbed on both titanium and zirconium tetravalent surface ions (g values in Table 3). The weaker g_{zz} component (g=2.030) corresponds to superoxide ions adsorbed on Zr^{4+}, while the more abundant one (g=2.022) is due to O_2^- on top of Ti^{4+} ions.[43] This finding indicates that both zirconium and titanium ions are exposed at the surface.

Analyzing the two spectra (before and after O_2 absorption) in quantitative terms it can be noted that the integrated intensity of the EPR signal of the reduced sample (Figure 12a) is one order of magnitude higher than that of the sample contacted with oxygen (Figure 12b). The difference is due to the fact that the majority of oxygen captured by the annealed material is reduced to a diamagnetic form (see equation 4) and is likely used to restore the losses caused by annealing. Only a minor fraction of the adsorbed oxygen remains partially reduced to superoxide. The sequence leading to O_2 incorporation is that typical of reducible oxides

$$O_2 + e^- \rightarrow O_2^- + e^- \rightarrow O_2^{2-} + 2e^- \rightarrow 2O^{2-} \qquad (4)$$

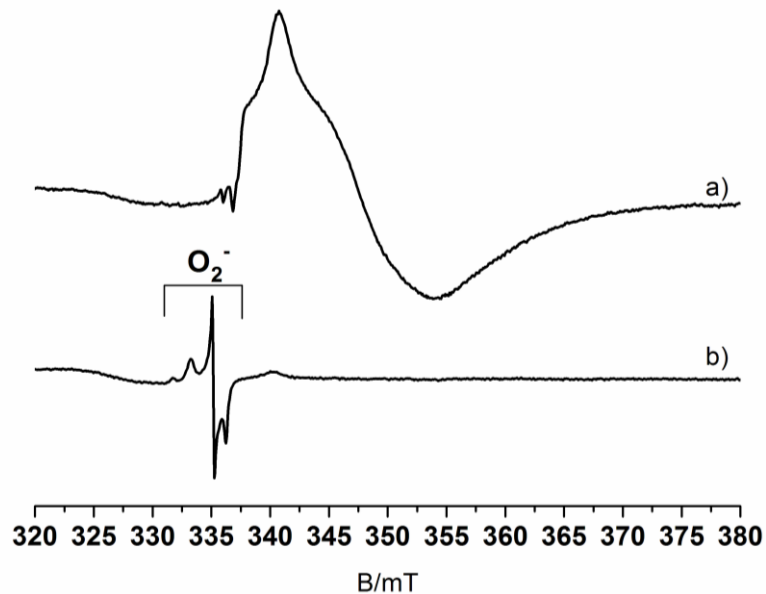where the only paramagnetic product is indeed O_2^-, at the first step.

Figure 12. EPRspectra of a) ZT powder reduced 1 hour at 873 K under vacuum and b) sample in a) contacted with O_2. Both spectra were recorded at 77 K and with a microwave power of 10 mW.
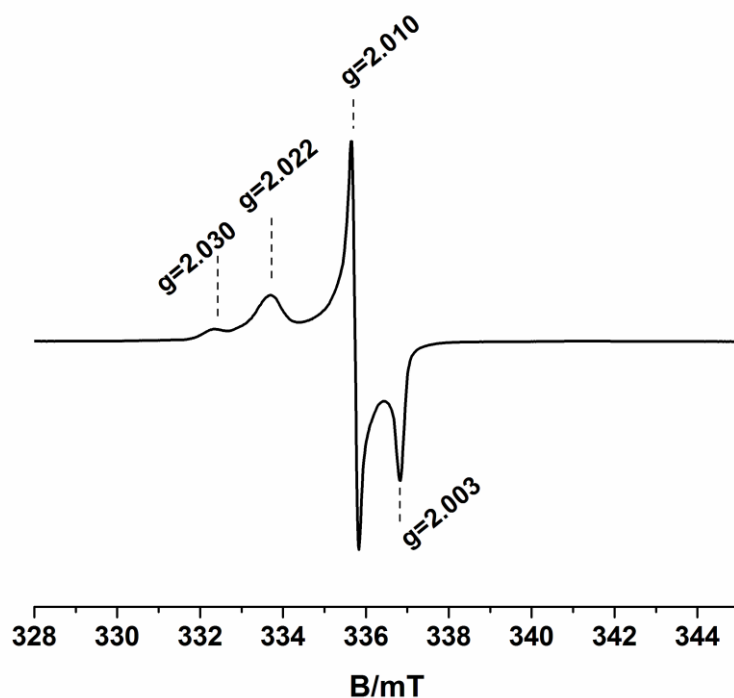
Figure 13. Magnification ofEPR spectrum of superoxide radical formed contacting the ZT sample annealed at 873 K with oxygen. The spectrum was recorded at 77 K and with a microwave power of 1 mW

Table 3. g value of superoxide species adsorbed on ZT sample extracted by simulation performed using SIM32 software.[44]

g_{zz}	g_{yy}	g_{xx}	description
2.022 ± 0.002	2.010 ± 0.0005	2.003 ± 0.0005	O_2^- on Ti^{4+}
2.030 ± 0.002	2.010 ± 0.0005	2.003 ± 0.0005	O_2^- on Zr^{4+}

3.4.2.   Photoinduced charge separation.

The photoactivity of $ZrTiO_4$ has been tested by EPR under UV-vis irradiation. By EPR it is in principle possible to monitor the formation and stabilization of both photoexcited electrons and holes.[45]

Irradiation under vacuum of the activated solid (showing a weak trace of Zr^{3+} impurities (Figure 14a) causes the appearance of distinct, but partially overlapped, signals (Figure 14b). In the region at $g<g_e$ (right hand side of the spectrum) trapping of photoexcited electrons is manifested by the increase of isolated Zr^{3+} ions and Ti^{3+} (broad signal amenable to surface species [46]). At lower field

20

($g>g_e$) the axial signal, characterized by the g components $g_1=2.005$ and $g_2=2.014$, corresponds to trapped holes (O^- ions).

In the spectrum c of Figure 14, which reports the sample after a thaw-freeze treatment (lamp off, heating at room temperature and cooling again at 77 K), the signals belonging to the holes and Zr^{3+} ions are still appreciable though with lower intensity. The majority of holes and electrons therefore recombine and in particular the electrons, stabilized on Ti^{3+}, undergo a complete recombination upon temperature increasing. Comparing the intensities of the three spectra in Figure 14 it can be concluded that a fraction of the charge trapping sites escapes recombination. Isolated Zr^{3+} (Figure 14c) in fact recombine less efficiently than Ti^{3+}.
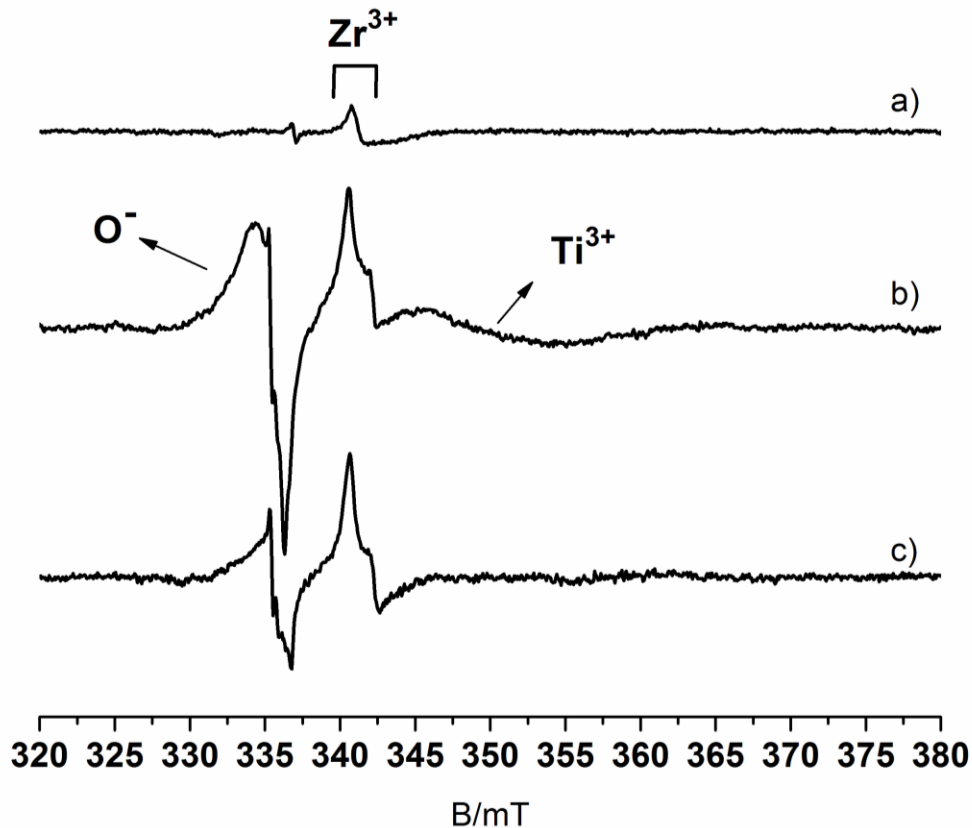

Figure 14. EPR spectra showing the effect of UV-vis irradiation under vacuum of zirconium titanate. a) activated sample in dark, b) after UV-vis irradiation, c) sample after a thaw-freeze treatment aimed to observe charge recombination (lamp off, heating at RT and cooling again at 77 K). All the spectra are recorded at 77 K with a microwave power of 10 mW. The irradiation was performed in the EPR cavity at 77 K for 10 minutes with a UV-vis light.

The calculated VB-CB excitation, in fact, leads to a hole localized on an O ion and an electron fully localized on the 3d state of a Ti atom, as clearly shown in the spin density in Figure 15. This triplet excited state is about 3 eV above the singlet ground state.
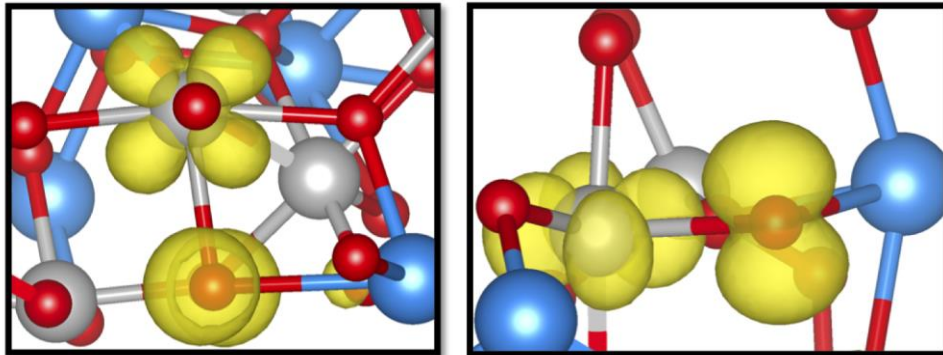

Figure 15. Top and side views of the spin density plot of 2-$ZrTiO_4$ VB-CB excitation (triplet excited state) (isolevel cutoff 0.008).

3.4.3.   Surface trapping of photogenerated carriers.

An important feature of an efficient photocatalyst is related to the capability of the photo-generated charge to reach the surface of the nanoparticles. For this reason irradiation of $ZrTiO_4$ under oxygen atmosphere was performed. The gas phase O_2 molecule, indeed, reacts with those photo-generated electrons capable of reaching the surface, producing surface adsorbed superoxide O_2^-:

$$O_{2(gas)} + e^-_{(CB)} \rightarrow O_2^-{}_{(ads)} \qquad (5)$$
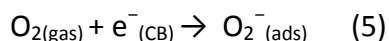
The formation of O_2^- upon irradiation under O_2, is thus the evidence of generation of surface reacting electrons. Figure 16 shows the EPR spectra after the UV-vis irradiation of the ZT sample in atmosphere of O_2. The trace of Zr^{3+} in the starting material (Figure 16a) are not altered by contact with O_2 (Figure 16b) nor by the irradiation (Figure 16c). After irradiation with UV-vis light, however, an intense signal typical of superoxide ions appears (Figure 16c).

The feature of the EPR spectrum of the superoxide radical formed upon irradiation is strictly similar to that observed upon reoxidation (Figure 11 and Figure 12) and is due to the superoxide ions adsorbed on both Ti^{4+} and Zr^{4+} ions present at the surface of the solid.
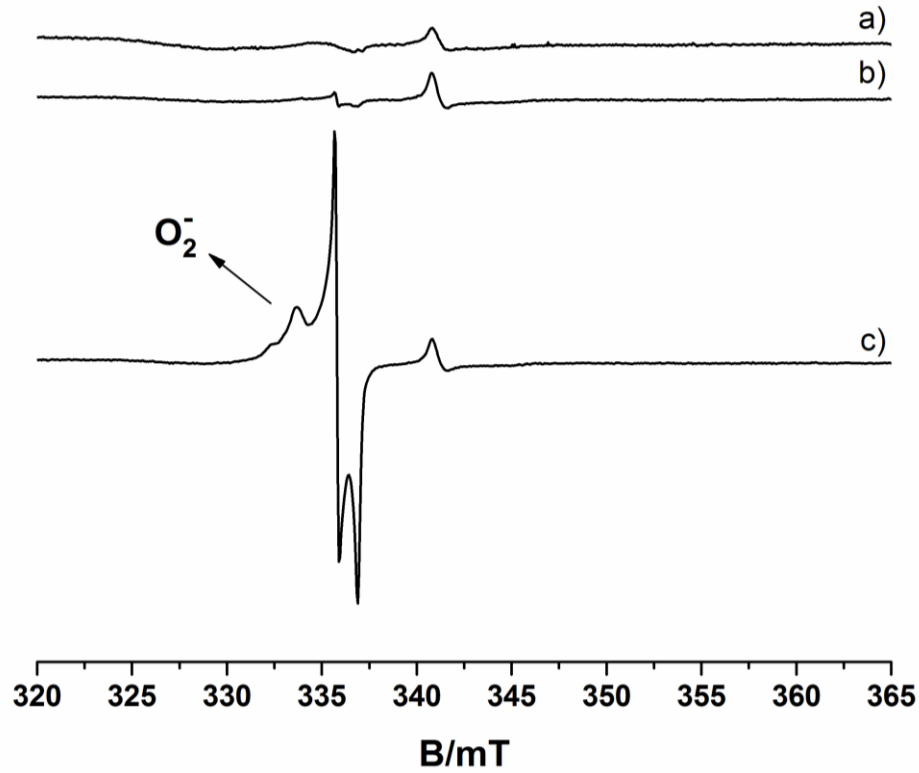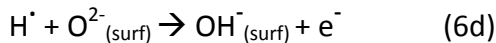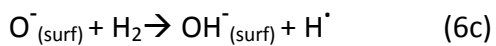
Figure 16. EPR spectra of a ZT sample irradiated in O_2 atmosphere: a) activated sample in dark, b) the same sample contacted with 20mbar of O_2 in dark, c) sample in b) upon irradiation with UV-vis light at 77 K. All the spectra were recorded at 77 K and with a microwave power of 1 mW.

In a parallel experiment, the ZT sample has been irradiated with UV-vis light in a H_2 atmosphere to produce reactive H atoms. Under such conditions, the holes photo-generated in the valence band migrate to the surface, where they interact with molecular hydrogen (H_2) that undergoes a homolytic splitting generating reactive hydrogen atoms. H˙ atoms, in turn, react at the surface, injecting electrons into the solid (reactions 6 a-c).[47]

$$MO_x + h\nu \rightarrow e^-_{(CB)} + h^+_{(VB)} \qquad (6a)$$

$$h^+_{(VB)} + O^{2-}_{(surf)} \rightarrow O^-_{(surf)} \qquad (6b)$$

$$O^-_{(surf)} + H_2 \rightarrow OH^-_{(surf)} + H˙ \qquad (6c)$$

$$H˙ + O^{2-}_{(surf)} \rightarrow OH^-_{(surf)} + e^- \qquad (6d)$$
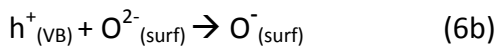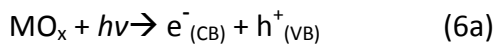
The fingerprint of surface hole reactivity is thus the formation of reduced species due to the electron generated according to equation 6d.

The effects on the EPR spectra of the irradiation in H_2 atmosphere are reported in Figure 16. The background spectrum (Figure 17a) doesn't change contacting the powder with of H_2 (Figure 17b). However, upon UV-vis irradiation in presence of H_2 (Figure 17c) a new very intense signal typical of Ti^{3+}, and already discussed in previous sections, arises. The signal encompasses those Ti^{3+} formed both by trapping the photogenerated electrons and those formed by the series of reactions listed above (6) and terminated by electron injection and trapping. By irradiation under H_2, Ti^{3+} centers are thus formed so that no more recombination is possible as shown by the fact that, upon thaw-freeze treatment, the spectrum remains unaffected (Figure 17d).

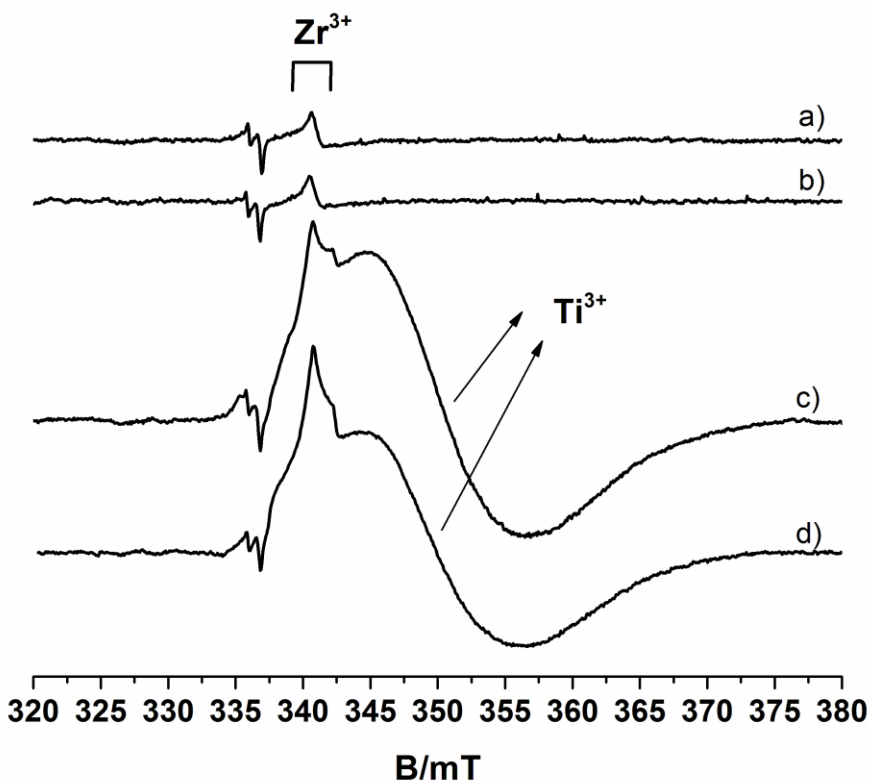**Figure 17.** EPR spectra of ZT sample irradiated in H_2 atmosphere: a) activated sample, b) sample in a) contacted with 50 mbar of H_2, c) sample in b) upon irradiation with UV-vis light at 77 K in H_2 atmosphere, d) sample after a thaw-freeze treatment (lamp off, heating at RT and cooling again at 77 K). All the spectra were recorded at 77 K and with a microwave power of 10 mW.

4. CONCLUSIONS

Nanometric zirconium titanate crystals with equivalent content of the two metal ions ($ZrTiO_4$) are easily prepared by sol-gel chemistry. This solid is interesting in that it introduces an elevated concentration of tetravalent zirconium ions in a matrix that, under the structural point of view, is essentially TiO_2-like, being based on linked MeO_6 octahedrons (Me= Zr, Ti) with three coordinated oxygen ions at the connection. Zirconium ions in $ZrTiO_4$ are thus inserted in a matrix strongly differing from that of ZrO_2, which has a fluorite (or a modified fluorite) structure with cations in cubic (or distorted cubic) coordination depending on the polymorph. The possible changes in both the band-gap energy value (E_g) and the conduction band potential of titanium dioxide (E_g = 3.0 eV for rutile and 3.2 eV for anatase), caused by the presence of zirconium ions (E_g = 5 eV for zirconia), prompted us to investigate the photophysical and photochemical properties of this solid. The band potential of the TiO_2 conduction band is only slightly more negative, in fact, than the NHE potential, whereas that of ZrO_2 is markedly more negative. A system maintaining the general photocatalytic properties of titania (mainly the photooxidation ability related to the holes in the valence band) simultaneously increasing its reductive abilities should be of remarkable interest in the area of photocatalysis. The picture arising from both experiments and calculations reveals the band gap value of 3.65 evaluated from the optical spectra is 14% higher than that of anatase. A quite similar result is obtained by calculations. In fact, once scaled of the well-known overestimation typical of the B3LYP functional, the calculated E_g value of zirconium titanate also falls at a value in between those of the two binary oxides (TiO_2, ZrO_2) but definitely closer to that of titania. Both TiO_2 and $ZrTiO_4$ have a similar composition of the conduction band (formed by Ti 3d orbitals, Figure 8) but the latter has a slightly larger E_g (by 0.45 eV) due to structural effects. The alignment of the band potential of $ZrTiO_4$ with those of the two binary reference oxides has been done following the procedure reported by Butler [48] and based on the Mulliken electronegativity of the elements (Figure 18). The result obtained for both TiO_2 and ZrO_2 are close to what has been found for the same oxides in various reports.[49-51] The valence band edge of $ZrTiO_4$ results in this way slightly more positive than that of TiO_2 (0.25 eV) thus, on the basis of the energy gap value the limit of the conduction band of the solid is about 0.20 eV more negative of the corresponding one of titania (Figure 18). Preliminary results by Ultraviolet Photoelectron Spectroscopy (UPS) are in

agreement with the reported picture. In other words, the position of the conduction band edge is not midway between those of the two reference oxides but closer to that of titania. Nonetheless the presence of a small but definite increment of the reductive potential of conduction band electrons in $ZrTiO_4$ with respect to TiO_2 can be confidently assumed.
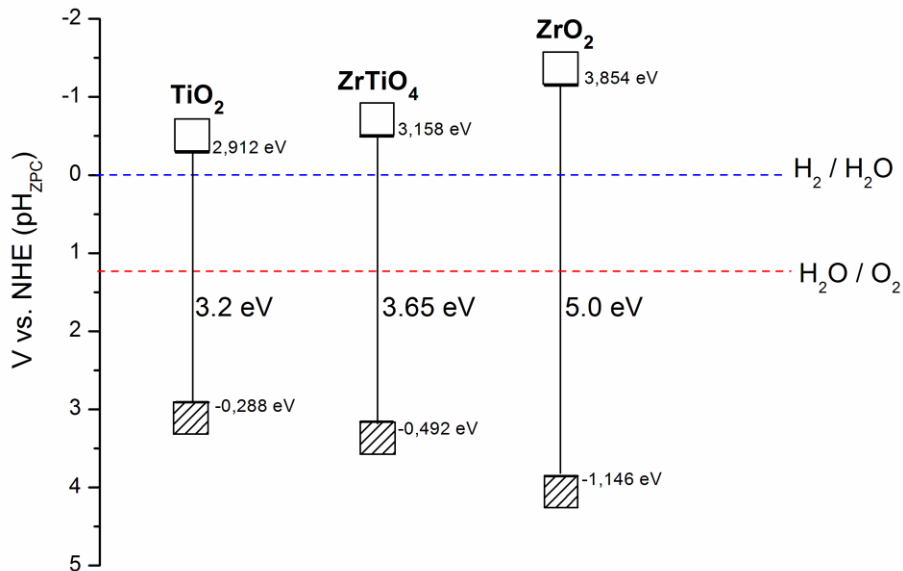

Figure 18. Relationship between band structure of ZrO_2, TiO_2 and $ZrTiO_4$ and redox potentials of water splitting.

Zirconium titanate is not a highly reducible oxide. Its properties upon vacuum annealing at increasing temperature, in terms of oxygen vacancies formation, show a dual behaviour. In the lower temperature range (RT-673 K) ZT behaviour is close to that of zirconium dioxide with no or few oxygen vacancies formation, as we have shown in terms of absence of excess electrons after annealing. It is well known that titanium dioxide behaves differently forming oxygen vacancies and excess electrons since the early stages of annealing.[41] Over 673 K, however, the oxygen loss in $ZrTiO_4$ is stronger with formation of reduced Ti^{3+} centers which are monitored by EPR (Figure 10). The behaviour of $ZrTiO_4$ upon annealing at high temperature is due to the presence of tetravalent Ti ions, which are better electron traps than the Zr ions since their electronic energy is lower. The computational results nicely fit with the experimental observations explaining the initial resistance to oxygen loss in terms of the formation cost of an oxygen vacancy that, in $ZrTiO_4$, is 1.5 eV higher

than in TiO_2. The formation of Ti^{3+} upon annealing at higher temperature is also accounted for by calculations that indicate that, after O extraction, the most stable solution is that with two electrons on two distinct titanium ions (Table 2).

The low energy of the titanium states that occupy the bottom of the conduction band also explains the behaviour of the solid upon irradiation under vacuum with localization of the photogenerated electrons preferentially on Ti ions located at the surface of the nanocrystals, as indicated by the very broad linewidth of the EPR signal (Figure 14b). Actually the EPR spectrum indicates also the formation of a fraction of reduced Zr^{3+} ions which, surprisingly, are less capable of recombining with the holes.

Summarizing zirconium titanate is an oxide that could be potentially useful in photocatalysis since we have demonstrated that it is photosensitive and easily undergoes charge separation when irradiated with photons with energy higher than the band gap value (3.65 eV, ca. 340 nm, Figure 14) and that the photogenerated charge carriers easily reach the surface and react with molecules in the gas phase (Figure 16 and Figure 17). In this kind of experiments the behaviour of the titanate is similar to that of titanium dioxide, the benchmark system in photocatalysis for pollutants abatement.

In conclusion the interest in the relatively unexplored zirconium titanate is due to its band potentials that differ from those of TiO_2 while the structure is strongly reminiscent of that of titania. Particularly interesting is the conduction band potential, which is more negative (about 0.2 eV) than that of anatase, thus a higher reductive potential of photoexcited electrons is expected, making this material a possible candidate for hydrogen evolution via water photoreduction.[52,53]

SUPPORTING INFORMATION

2x2x2 Supercell of 1-, 2-, 3- and 4-ZrTiO$_4$ optimized structures and calculated electronic bands of ZrTiO$_4$ are reported in Supporting information.

REFERENCES

1. Serpone, N.; Emeline, A. V., Semiconductor Photocatalysis - Past, Present, and Future Outlook. *J. Phys. Chem. Lett.* **2012**, *3*, 673-677.

2. Lewis, N. S., Light Work with Water. *Nature* **2001**, *414*, 589-590.

3. Reddy, B. M.; Khan, A., Recent Advances on TiO_2-ZrO_2 Mixed Oxides as Catalysts and Catalyst Supports. *Catal. Rev. Sci. Eng.* **2005**, *47*, 257-296.

4. Linsebigler, A. L.; Lu, G.; Yates Jr, J. T., Photocatalysis on TiO_2 Surfaces: Principles, Mechanisms, and Selected Results. *Chem. Rev.* **1995**, *95*, 735-758.

5. Kohno, Y.; Tanaka, T.; Funabiki, T.; Yoshida, S., Photoreduction of CO_2 with H_2 Over ZrO_2. A Study on Interaction of Hydrogen with Photoexcited CO_2. *Phys. Chem. Chem. Phys.* **2000**, *2*, 2635-2639.

6. Gionco, C.; Paganini, M. C.; Chiesa, M.; Maurelli, S.; Livraghi, S.; Giamello, E., Cerium Doped Zirconium Dioxide as a Potential New Photocatalytic Material. The Role of the Preparation Method on the Properties of the Material. *Appl. Catal., A* **2015**, *504*, 338-343.

7. Gionco, C.; Paganini, M. C.; Giamello, E.; Burgess, R.; Di Valentin, C.; Pacchioni, G., Cerium-Doped Zirconium Dioxide, a Visible-Light-Sensitive Photoactive Material of Third Generation. *J. Phys. Chem. Lett.* **2014**, *5*, 447-451.

8. Lopez, T.; Alvarez, M.; Tzompantzi, F.; Picquart, M., Photocatalytic Degradation of 2,4-Dichlorophenoxiacetic Acid and 2,4,6-Trichlorophenol with ZrO_2 and Mn/ZrO_2 Sol-Gel Materials. *J. Sol-Gel Sci. Technol.* **2006**, *37*, 207-211.

9. Troitzsch, U.; Ellis, D. J., The ZrO_2-TiO_2 Phase Diagram. *J. Mater. Sci.* **2005**, *40*, 4571-4577.

10. McHale, A.; Roth, R. S., Low-Temperature Phase Relationships in the System ZrO_2-TiO_2. *J. Am. Ceram. Soc.* **1986**, *69*, 827-832.

11. Brown, F. H.; Duwez, P., The Zirconia-Titania System. *J. Am. Ceram. Soc.* **1954**, *37*, 129-132.

12. Newnham, R. E., Crystal Structure of $ZrTiO_4$. *J. Am. Ceram. Soc.* **1967**, *50*, 216-216.

13. Pol, S.; Pol, V.; Gedanken, A.; Spijksma, G.; Grinblat, J.; Selvan, R. K.; Kessler, V.; Seisenbaeva, G.; Gohil, S., Synthesis of Nanocrystalline Zirconium Titanate and Its Dielectric Properties. *J. Phys. Chem. C* **2007**, *111*, 2484-2489.

14. Kim, D.-S.; Park, D.-H.; Kim, G.-D.; Choi, S.-Y., Dielectric Properties of $ZrTiO_4$ Thin Films Synthesized by Sol-Gel Method. *Met. Mater. Int.* **2004**, *10*, 361-365.

15. Lessing, P.; Yang, Z.; Miller, G.; Yamada, H., Corrosion of Metal Oxide Ceramics in Molten Lithium-Potassium Carbonates. *J. Electrochem. Soc.* **1988**, *135*, 1049-1057.

16. Park, Y., $Zr_{0.98}Sn_{0.02}TiO_4$ Single Crystal in a Low Electric Field: Birefringence, Dielectric, and Synchrotron X-Ray Studies. *Phys. Rev. B* **2000**, *62*, 8794-8801.

17. Leoni, M.; Viviani, M.; Battilana, G.; Fiorello, A. M.; Viticoli, M., Aqueous Synthesis and Sintering of Zirconium Titanate Powders for Microwave Components. *J. Eur. Ceram. Soc.* **2001**, *21*, 1739-1741.

18. Bianco, A.; Gusmano, G.; Freer, R.; Smith, P., Zirconium Titanate Microwave Dielectrics Prepared Via Polymeric Precursor Route. *J. Eur. Ceram. Soc.* **1999**, *19*, 959-963.

19. Chang, D. A.; Lin, P.; Tseng, T. Y., Optical Properties of $ZrTiO_4$ Films Grown by Radio-Frequency Magnetron Sputtering. *J. Appl. Phys.* **1995**, *77*, 4445-4451.

20. Hsu, C.-H.; Lin, S.-Y., Characterization of $ZrTiO_4$ Thin Films Prepared by Sol-Gel Method. *Mater. Sci. Semicond. Process.* **2013**, *16*, 1262-1266.

21. Cosentino, I. C.; Muccillo, E. N. S.; Muccillo, R., Development Of Zirconia-Titania Porous Ceramics For Humidity Sensors. *Sens. Actuators, B* **2003**, *96*, 677-683.

22. Dondi, M.; Matteucci, F.; Cruciani, G., Zirconium Titanate Ceramic Pigments: Crystal Structure, Optical Spectroscopy and Technological Properties. *J. Solid State Chem.* **2006**, *179*, 233-246.

23. Devi, K. B.; Singh, K.; Rajendran, N., Sol-Gel Synthesis and Characterisation of Nanoporous Zirconium Titanate Coated on 316L SS for Biomedical Applications. *J. Sol-Gel Sci. Technol.* **2011**, *59*, 513-520.

24.   Navio, J.; Colòn, G., Heterogeneous Photocatalytic Oxidation of Liquid Isopropanol by TiO_2, ZrO_2 And $ZrTiO_4$ Powders. *Stud. Surf. Sci. Catal.* **1994**, *82*, 721-728.

25.   Navio, J.; Hidalgo, M.; Roncel, M.; De la Rosa, M., A Laser Flash Photolysis Study of the Photochemical Activity of a Synthesised $ZrTiO_4$: Comparison with Parent Oxides, TiO_2 and ZrO_2. *Mater. Lett.* **1999**, *39*, 370-373.

26.   Navio, J.; Colon, G.; Herrmann, J., Photoconductive and Photocatalytic Properties of $ZrTiO_4$. Comparison with the Parent Oxides TiO_2 and ZrO_2. *J. Photochem. Photobiol., A* **1997**, *108*, 179-185.

27.   Manrìquez, M.; Lòpez, T.; Aguilar, D.; Quintana, P., Phase Structure and Thermal Evolution in Mixed Oxide TiO_2-ZrO_2 Powders Obtained by the Sol-Gel Process. In *Emerging Fields in Sol-Gel Science and Technology*, Springer: 2003; pp 254-264.

28.   http://cimewww.epfl.ch/people/stadelmann/jemswebsite/jems.html.

29.   Bernal, S.; Botana, F. J.; Calvino, J. J.; Lòpez-Cartes, C.; Pérez-Omil, J. A.; Rodrìguez-Izquierdo, J. M., The Interpretation of HRTEM Images of Supported Metal Catalysts Using Image Simulation: Profile View Images. *Ultramicroscopy* **1998**, *72*, 135-164.

30.   Pérez-Omil, J. A. Doctoral thesis. University of Cádiz, Spain, 1994.

31.   Becke, A. D., Density-Functional Thermochemistry. III. The Role of Exact Exchange. *J. Chem. Phys.* **1993**, *98*, 5648-5652.

32.   Lee, C.; Yang, W.; Parr, R. G., Development of the Colle-Salvetti Correlation-Energy Formula into a Functional of the Electron Density. *Phys. Rev. B* **1988**, *37*, 785-789.

33.   Dovesi, R.; Saunders, V.; Roetti, C.; Orlando, R.; Zicovich-Wilson, C.; Pascale, F.; Civalleri, B.; Doll, K.; Harrison, N.; Bush, I., CRYSTAL14 Users Manual. *University of Torino, Torino* **2014**.

34.   Siggel, A.; Jansen, M., $ZrSn_{0.5}Ti_{0.5}O_4$ as a Matrix for Ceramic Colors- Structural Investigations on $ZrTiO_4$ $ZrSn_{0.5}Ti_{0.5}O_4$ *Z. Anorg. Allg. Chem.* **1990**, *582*, 93-102.

35.   Troitzsch, U.; Christy, A. G.; Ellis, D. J., The Crystal Structure of Disordered $(Zr,Ti)O_2$ Solid Solution Including Srilankite: Evolution Towards Tetragonal ZrO_2 with Increasing Zr. *Phys. Chem. Miner.* **2005**, *32*, 504-514.

36.   French, R.; Glass, S.; Ohuchi, F.; Xu, Y.-N.; Ching, W., Experimental and Theoretical Determination of The Electronic Structure and Optical Properties of Three Phases of ZrO_2. *Phys. Rev. B* **1994**, *49*, 5133-5142.

37.   Kowalczyk, S.; McFeely, F.; Ley, L.; Gritsyna, V.; Shirley, D., The Electronic Structure of $SrTiO_3$ and Some Simple Related Oxides (MgO, Al_2O_3, SrO, TiO_2). *Solid State Commun.* **1977**, *23*, 161-169.

38.   Di Valentin, C.; Pacchioni, G.; Selloni, A., Reduced and n-type Doped TiO_2: Nature of Ti^{3+} Species. *J. Phys. Chem. C* **2009**, *113*, 20543-20552.

39.   Gionco, C.; Paganini, M. C.; Giamello, E.; Burgess, R.; Di Valentin, C.; Pacchioni, G., Paramagnetic Defects in Polycrystalline Zirconia: An EPR and DFT Study. *Chem. Mater.* **2013**, *25*, 2243-2253.

40.   Calatayud, M.; Markovits, A.; Menetrey, M.; Mguig, B.; Minot, C., Adsorption on Perfect and Reduced Surfaces of Metal Oxides. *Catal. Today* **2003**, *85*, 125-143.

41.   Livraghi, S.; Chiesa, M.; Paganini, M. C.; Giamello, E., On the Nature of Reduced States in Titanium Dioxide As Monitored by Electron Paramagnetic Resonance. I: The Anatase Case. *J. Phys. Chem. C* **2011**, *115*, 25413-25421.

42.   Albanese, E.; Leccese, M.; Di Valentin, C.; Pacchioni, G., Magnetic Properties of Nitrogen-Doped ZrO_2: Theoretical Evidence of Absence of Room Temperature Ferromagnetism. *Sci. Rep.* **2016**, *6*, 31435.

43.   Anpo, M.; Che, M.; Fubini, B.; Garrone, E.; Giamello, E.; Paganini, M. C., Generation of Superoxide Ions at Oxide Surfaces. *Top. Catal.* **1999**, *8*, 189-198.

44.   Adamski, A.; Spałek, T.; Sojka, Z., Application of EPR Spectroscopy for Elucidation of Vanadium Speciation In VO_x/ZrO_2 Catalysts Subject to Redox Treatment. *Res. Chem. Intermed.* **2003**, *29*, 793-804.

45.   Chiesa, M.; Paganini, M. C.; Livraghi, S.; Giamello, E., Charge trapping in TiO_2 polymorphs as seen by Electron Paramagnetic Resonance spectroscopy. *Physical Chemistry Chemical Physics* **2013**, *15*, 9435-9447.

46.   Livraghi, S.; Rolando, M.; Maurelli, S.; Chiesa, M.; Paganini, M. C.; Giamello, E., Nature of Reduced States in Titanium Dioxide as Monitored by Electron Paramagnetic Resonance. II: Rutile and Brookite Cases. *J. Phys. Chem. C* **2014**, *118*, 22141-22148.

47.　Berger, T.; Diwald, O.; Knozinger, E.; Napoli, F.; Chiesa, M.; Giamello, E., Hydrogen Activation at TiO_2 Anatase Nanocrystals. *Chem. Phys.* **2007**, *339*, 138-145.

48.　Butler, M. A.; Ginley, D. S., Prediction of Flatband Potentials at Semiconductor-Electrolyte Interfaces from Atomic Electronegativities. *J. Electrochem. Soc.* **1978**, *125*, 228-232.

49.　Marschall, R., Semiconductor Composites: Strategies for Enhancing Charge Carrier Separation to Improve Photocatalytic Activity. *Adv. Funct. Mater.* **2014**, *24*, 2421-2440.

50.　Li, J. T.; Wu, N. Q., Semiconductor-Based Photocatalysts and Photoelectrochemical Cells for Solar Fuel Generation: a Review. *Catal. Sci. Technol.* **2015**, *5*, 1360-1384.

51.　Chen, X. B.; Li, C.; Gratzel, M.; Kostecki, R.; Mao, S. S., Nanomaterials for Renewable Energy Production and Storage. *Chem. Soc. Rev.* **2012**, *41*, 7909-7937.

52.　Poston, M. J.; Aleksandrov, A. B.; Sabo, D. E.; Zhang, Z. J.; Orlando, T. M., UV Photon-Induced Water Decomposition on Zirconia Nanoparticles. *J. Phys. Chem. C* **2014**, *118*, 12789-12795.

53.　Jitputti, J.; Suzuki, Y.; Yoshikawa, S., Synthesis of TiO_2 Nanowires and Their Photocatalytic Activity for Hydrogen Evolution. *Catal. Commun.* **2008**, *9*, 1265-1271.

TOC Graphic